CONDENSED MATTER PHYSICS

Magnetization switching using topological surface states

Peng Li[1]*, James Kally[2]*, Steven S.-L. Zhang[3], Timothy Pillsbury[2], Jinjun Ding[1], Gyorgy Csaba[4], Junjia Ding[3], J. S. Jiang[3], Yunzhi Liu[5], Robert Sinclair[5], Chong Bi[6], August DeMann[1], Gaurab Rimal[7†], Wei Zhang[8,3], Stuart B. Field[1], Jinke Tang[7], Weigang Wang[6], Olle G. Heinonen[3], Valentine Novosad[3], Axel Hoffmann[3], Nitin Samarth[2], Mingzhong Wu[1‡]

Topological surface states (TSSs) in a topological insulator are expected to be able to produce a spin-orbit torque that can switch a neighboring ferromagnet. This effect may be absent if the ferromagnet is conductive because it can completely suppress the TSSs, but it should be present if the ferromagnet is insulating. This study reports TSS-induced switching in a bilayer consisting of a topological insulator Bi_2Se_3 and an insulating ferromagnet $BaFe_{12}O_{19}$. A charge current in Bi_2Se_3 can switch the magnetization in $BaFe_{12}O_{19}$ up and down. When the magnetization is switched by a field, a current in Bi_2Se_3 can reduce the switching field by ~4000 Oe. The switching efficiency at 3 K is 300 times higher than at room temperature; it is ~30 times higher than in Pt/$BaFe_{12}O_{19}$. These strong effects originate from the presence of more pronounced TSSs at low temperatures due to enhanced surface conductivity and reduced bulk conductivity.

INTRODUCTION

Materials with strong spin-orbit coupling can convert a charge current to a spin current and vice versa. Heavy metals, such as Pt and Ta, are one class of these materials in which the spin-orbit coupling is associated with the spin Hall effect in the bulk or the interfacial Rashba effect. When a heavy metal film is interfaced with a ferromagnetic (FM) film, the spin-orbit coupling-produced spin current in the heavy metal can exert a torque on the magnetization in the FM film, which is the so-called spin-orbit torque (SOT). This SOT effect can be used to switch magnetization (*1*–*3*), drive domain wall motion (*4*), or excite magnetization precession (*5*). This SOT-driven manipulation is not only of great fundamental interests but also of technological significance, and because of its high potential in energy-efficient memory and logic device applications.

Because of the spin-momentum locking of their topological surface states (TSSs), topological insulators (TIs) are expected to host spin-orbit coupling that is considerably stronger than in heavy metals and can thereby produce substantially larger SOT. Very recently, there have been a number of experimental demonstrations of SOT-induced magnetization switching in TI/FM bilayered structures (*6*–*12*). The TI materials used in those experiments included Bi_2Se_3 (*7*, *8*, *11*), $(Bi_{1-x}Sb_x)_2Te_3$ (*6*, *9*), $Bi_{0.9}Sb_{0.1}$ (*12*), and SmB_6 (*10*), while the FM materials ranged from magnetically doped TIs (*6*, *9*) to ferrimagnetic alloys (*7*) and FM metals (*8*, *10*–*12*). The demonstrated switching efficiencies were all higher than in the heavy metal/FM counterparts, which provide substantial implications for future applications of TI materials.

The FM films in those studies, however, were all conductive with conductivities either about one order of magnitude higher than (*7*, *8*, *10*–*12*) or comparable to the conductivities of the TI films (*6*, *9*). A straightforward consequence of this is the severe shunting current in the FM film, which not only limits the switching efficiency but also may cause certain thermal issues, as discussed in (*13*). Besides the shunting current, the conductive nature of the FM components has a much more serious consequence—the TSSs may have been largely spoiled by the FM films and may not account for the observed strong SOT effects. Previous works have shown that interfacing a TI with a conductive FM film can result in a significant modification or even complete suppression of the TSSs in the TI (*14*–*18*). On one hand, experimental studies showed that the deposition of an Fe layer on a Bi_2Se_3 film not only largely lowered the energy of the surface states but also introduced additional surface bands in the bulk gap (*14*), while the growth of an Fe film on a α-Sn film completely suppressed the TSSs in the α-Sn (*15*). On the other hand, analyses using density functional theory and tight-binding models have shown that the charge transfer and hybridization effects at the interface between a TI and a conductive FM in a bilayered structure could push the Dirac point into the valence band and introduce additional surface states, as demonstrated experimentally, or completely destroy the helical spin texture of the surface states and thereby make the surface states trivial (*16*–*18*). These experimental and theoretical works together indicated that TSSs were unlikely to be responsible for the efficient SOT switching observed in the recent experiments (*6*–*12*).

One can eliminate the above issues simply by replacing the conductive FM components with insulating FM materials. In this aspect, note that a recent theoretical work compared the effects of conductive and insulating FM films on the TSSs in TI/FM heterostructures. It showed that, in stark contrast with the conductive FM case, the TSSs in a TI/magnetic insulator (MI) structure can be largely preserved except for opening of a small gap at the Dirac point when strong coupling exists at the interface (*16*). Thus, one can expect the

[1]Department of Physics, Colorado State University, Fort Collins, CO 80523, USA. [2]Department of Physics, Pennsylvania State University, University Park, PA 16802, USA. [3]Materials Science Division, Argonne National Laboratory, Lemont, IL 60439, USA. [4]Faculty of Information Technology and Bionics, Pazmany Peter Catholic University, Budapest, Hungary. [5]Department of Materials Science and Engineering, Stanford University, Stanford, CA 94305, USA. [6]Department of Physics, University of Arizona, Tucson, AZ 85721, USA. [7]Department of Physics and Astronomy, University of Wyoming, Laramie, WY 82071, USA. [8]Department of Physics, Oakland University, Rochester, MI 48309, USA.
*These authors contributed equally to this work.
†Present address: Department of Physics and Astronomy, Rutgers University, Piscataway, NJ 08854, USA.
‡Corresponding author. Email: mwu@colostate.edu

presence of bona fide TSSs in TI/MI structures and the possibility of purely TSS-driven SOT switching in the structures.

This study reports on the demonstration of TSS-induced switching in a TI/MI bilayered structure where the TI layer is a Bi_2Se_3 film consisting of six quintuple layers and the MI layer is a 5-nm-thick $BaFe_{12}O_{19}$ film that has a large magnetocrystalline anisotropy and shows an effective perpendicular anisotropy field of about 22 kOe. It is found that the switching response in the $BaFe_{12}O_{19}$ film strongly depends on the charge current applied to the Bi_2Se_3 film. When a constant magnetic field is applied in the film plane, the charge current in the Bi_2Se_3 film can switch the magnetization in the $BaFe_{12}O_{19}$ film between the up and down states. When the magnetization is switched by sweeping an obliquely applied magnetic field with a constant charge current in the Bi_2Se_3 film, the current can cause the switching field H_{sw} to decrease or increase, depending on the current polarity, by as much as 4000 Oe. A decrease in temperature (T) results in a monotonic reduction in the switching current in the field fixed measurements and a monotonic increase in the change of H_{sw} in the current fixed measurements. This result evidently indicates the presence of strong SOT responses at low T, while the latter can be attributed to the presence of strong TSSs due to enhanced surface state conductivity and decreased bulk state conductivity. When compared with Pt/$BaFe_{12}O_{19}$, the SOT efficiency is comparable at room temperature but is about 30 times higher at T = 3 K. These results demonstrate the merits of TSSs in manipulating magnetization and thereby shed light on the applications of TIs in spintronic devices.

RESULTS

Properties of Bi_2Se_3/$BaFe_{12}O_{19}$ samples

The data presented in this work were obtained using a Bi_2Se_3 (6 nm)/$BaFe_{12}O_{19}$ (5 nm) bilayer with properties shown in Figs. 1 and 2. Figure 1 presents the structural and electrical properties. Figure 1A shows an x-ray diffraction (XRD) spectrum measured on the $BaFe_{12}O_{19}$ film before the growth of the Bi_2Se_3 film. The spectrum shows a c-axis orientation of the film. Figure 1B gives a reflection high-energy electron diffraction (RHEED) image obtained in situ right after the growth of the Bi_2Se_3 film on the $BaFe_{12}O_{19}$ film. It shows notable streaks that confirm the epitaxial growth of the Bi_2Se_3 film. The epitaxial growth of the $BaFe_{12}O_{19}$ and Bi_2Se_3 films was further confirmed by cross-section high-resolution transmission electron microscopy imaging, as shown in fig. S6.

Figure 1D shows the Hall resistance (R_H) data that were measured using a Hall bar structure shown in Fig. 1C. One can see that (i) R_H decreases linearly with an increase in the magnetic field (H), indicating the n-type nature of the Bi_2Se_3 film, and (ii) the slope is larger at lower T. These characteristics are consistent with those reported previously for Bi_2Se_3 films (*19*). Figure 1E presents the sheet carrier density (n_{2D}) calculated from the R_H data; the calculation used $n_{2D} = -\frac{\mu_0 H}{e R_H}$ (*20*), where μ_0 is the permeability of free space and $-e$ is the elementary charge. The n_{2D} values in Fig. 1E are close to those reported previously for Bi_2Se_3 films with bulk conduction (*8*, *21*), indicating the presence of a noninsulating bulk in the Bi_2Se_3 film in the sample. The inset in Fig. 1E shows the Fermi level (E_F) relative to the Dirac point estimated using the n_{2D} data (see the Supplementary Materials); one can see that E_F drops as T decreases. The negative slopes shown in Fig. 1D, the magnitude of n_{2D} shown in Fig. 1E, and the drop of E_F with a decrease in T shown in the inset of Fig. 1E together indicate that E_F is in the bulk conduction band and moves toward the bottom of the conduction band with a decrease in T.

The moving of the E_F toward the conduction band bottom with decreasing T would generally lead to a reduced carrier density, but increased carrier mobility is expected at low T because electron-phonon scattering generally becomes weaker with a decrease in T. The competition of these two effects can give rise to a certain characteristic in the conductivity (σ) versus T response. Figure 1F presents the $\sigma(T)$ data measured using the same Hall bar. The inset shows the same data but only for the low-T range in a natural logarithm scale. The data show that σ increases with a decrease in T from 300 to about 25 K but then decreases with a further decrease in T. This response indicates that in the high-T range, the electron-phonon scattering overwhelms the E_F shifting effect, but in the low-T range, the E_F shifting plays a major role. This result can be understood in terms of the change of phonon density with T. The data in Fig. 1 (D to F) together indicate that the E_F moves toward the conduction band bottom with a decrease in T and thereby gives rise to a reduced bulk conductivity in the low-T regime (3 to 25 K). This result, together with low-T enhancement of surface state conductivity, leads to the presence of more prominent TSSs and stronger SOT at low T, which is discussed below.

Note that as T approaches 3 K, σ exhibits a much weaker T dependence, as shown in the inset of Fig. 1F. This is due to the onset of quantum corrections to the diffusive transport. In standard Bi_2Se_3 thin films, $\sigma(T)$ at very low T is expected to be logarithmic, namely, $\sigma(T)$~ln$T$, due to the presence of Coulomb interactions between the electrons (*22*, *23*) and quantum interference–associated weak antilocalization (*24*). Specifically, it is expected that, with a decrease in ln$T$, the electron-electron interaction reduces σ, while the weak antilocalization enhances σ. It should be mentioned that the proximity to $BaFe_{12}O_{19}$ may result in complex electrical behavior in Bi_2Se_3 due to the breaking of time reversal symmetry by interfacial exchange coupling; as shown below, the observation of the anomalous Hall effect (AHE) in the Bi_2Se_3 film indicates that electrons in Bi_2Se_3 are affected by the interfacial exchange. Unexpectedly, the data do not show any obvious consequences of this interfacial exchange on the quantum corrections. On one hand, the red line in the inset of Fig. 1F suggests a ln$T$ dependence of σ in the T range of 3.0-4.5 K. On the other hand, as shown in the Supplementary Materials, the magnetoresistance seems to follow the standard weak antilocalization-type field dependence (*24*, *25*). More extensive measurements over a wider T range below 3 K are required to systematically search for any effects of the interfacial exchange interaction on quantum corrections.

Figure 2 shows the magnetic properties and AHE resistance (R_{AHE}) of the samples. The data in Fig. 2 (A and B) show the magnetic properties of the $BaFe_{12}O_{19}$ film. The magnetization (M) vs. field (H) loops in Fig. 2A confirm the presence of a perpendicular magnetic anisotropy in the film, which is consistent with the c-axis orientation of the film shown by the data in Fig. 1A. The analysis of the loop data indicates a saturation induction of $4\pi M_s \approx 4.25$ kG, which is about 9.6% lower than the bulk value (4.70 kG), and an effective perpendicular anisotropy field of $H_u \approx 22$ kOe, which is about 29% higher than the bulk value (17 kOe). As shown in Fig. 2B, the saturation magnetization (M_s) data can be fitted well by the Bloch's law $M_s(T) = M_{s0}[1 - (T/T_c)^{3/2}]$, where M_{s0} denotes the value of M_s at T = 0 K and T_c is the Curie temperature. The $T^{3/2}$ dependence of $M_s(T)$ indicates a three-dimensional nature of the $BaFe_{12}O_{19}$ film,

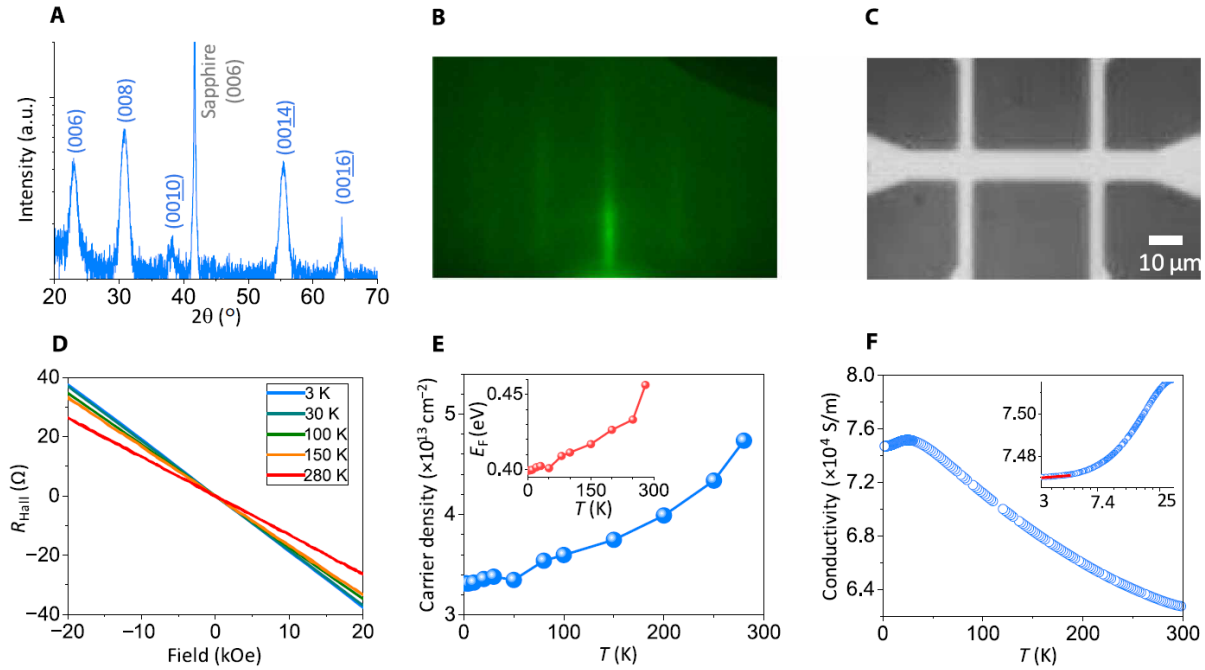

Fig. 1. Structural and electrical properties of $Bi_2Se_3/BaFe_{12}O_{19}$. (**A**) XRD spectrum of a 5-nm-thick $BaFe_{12}O_{19}$ film. a.u., arbitrary unit. (**B**) RHEED image of the Bi_2Se_3 film in a Bi_2Se_3 (6 nm)/$BaFe_{12}O_{19}$ (5 nm) sample. (**C**) Optical image of a $Bi_2Se_3/BaFe_{12}O_{19}$ Hall bar structure. (**D**) R_H of the Bi_2Se_3 film as a function of magnetic field at different temperatures (*T*), as indicated. (**E**) Sheet carrier density as a function of *T* was calculated using the R_H data in (D). The inset in (E) shows the E_F estimated from the carrier density data. (**F**) Conductivity of the Bi_2Se_3 film as a function of *T*. The inset in (F) shows the same data but in a natural logarithm scale. The data in (D) and (F) were measured using the Hall bar device shown in (C).

as opposed to the two-dimensional nature of ultrathin films with linear *T* dependence (*26*). The fitting yielded T_c = 751 K. This T_c is close to the bulk value (725 K). In contrast to M_s, the coercive field (H_c) or the (H_{sw}) remains almost unchanged over the entire *T* range, as shown in Fig. 2B, which is a desired feature in terms of device applications. These results together indicate that the $BaFe_{12}O_{19}$ film has properties close to those of the bulk materials despite the fact that it is only 5 nm thick.

When measured as a function of *H*, the R_H of the Hall bar structure consists of a linear background due to the ordinary Hall effect in the Bi_2Se_3 film and a hysteretic component due to the AHE also in the Bi_2Se_3 film. Figure 2 (C and D) presents R_{AHE} as a function of *H* for *T* = 300 K and *T* = 3 K, respectively. The data were obtained by subtracting the linear contribution from the initial R_H data, and the latter were measured by applying a weak alternating current (*I*ac) of 0.05 mA to the Hall bar. One can see that the $R_{AHE}(H)$ data in Fig. 2C show a hysteresis loop response similar to the $M(H)$ loop shown in Fig. 2A for a perpendicular field with two H_c values matching the corresponding values in Fig. 2A, as indicated by the vertical dashed lines. The comparison of the data in Fig. 2 (C and D) indicates that the H_c values at 3 K are very close to those at 300 K, consistent with the H_c data shown in Fig. 2B, while the R_{AHE} values at 3 K are slightly higher than those at 300 K, consistent with the trend of $M_s(T)$ shown in Fig. 2B. This similarity and consistency indicate that R_{AHE} scales with the normal component of the magnetization in the $BaFe_{12}O_{19}$ film and that one can probe the switching status in the $BaFe_{12}O_{19}$ film by simply measuring $R_{AHE}(H)$. It is important to mention that the AHE response usually occurs only in FM metals and that the presence of the AHE in the nonmagnetic Bi_2Se_3 film may originate from the magnetic proximity effect, as in other TI/MI systems (*27*–*29*), or by the effects of the imaginary part of the spin-mixing conductance at the interface (*30*) or the scattering of itinerant electrons in the Bi_2Se_3 film with the magnetic interface (*31*) as in heavy metal/MI systems.

SOT-induced switching in $Bi_2Se_3/BaFe_{12}O_{19}$

Figure 3 presents the data that demonstrate SOT-driven magnetization switching. As was the case for the R_{AHE} data presented above, the Hall measurements made use of a weak alternating current ($I_{ac} \approx 0.05$ mA), but before the measurement of each data point, a direct current (I_{dc}) was applied to the Hall bar for a duration of 5 ms. During the measurements, a constant external field **H** was applied along the *x* axis to tilt the magnetization **M** away from the perpendicular anisotropy axis (the *z* axis) and thereby assists the switching. This field also helps ensure deterministic switching. The data demonstrate that I_{dc} in the Bi_2Se_3 film can switch **M** in the $BaFe_{12}O_{19}$ film via the SOT $\boldsymbol{\tau}_{SO}$ (along the *y* axis).

Consider first the case shown by the blue data points in Fig. 3B, for which **M** is initially in the "up" state and I_{dc} is swept from positive to negative. When $I_{dc} > 0$, $\boldsymbol{\tau}_{SO}$ produces a field, shown as $\mathbf{H}_{SO+}$ in Fig. 3A, that tends to rotate **M** toward the anisotropy field $\mathbf{H}_u$. In this regime, **M** remains in the "up" state and R_{AHE} is positive. When I_{dc} becomes negative, the spin polarization on the Bi_2Se_3 surface reverses direction and accordingly $\boldsymbol{\tau}_{SO}$ changes its direction, giving rise to an SOT field, which is indicated by $\mathbf{H}_{SO-}$ in Fig. 3A. When sufficiently strong, $\mathbf{H}_{SO-}$ can switch **M** to the "down" state; this switching is indicated by the sign change of R_{AHE} shown in Fig. 3B. When I_{dc} is swept from negative to positive, an inverse process occurs and the SOT field switches **M** back to the "up" state, which is indicated by the change of R_{AHE} from negative to positive shown by

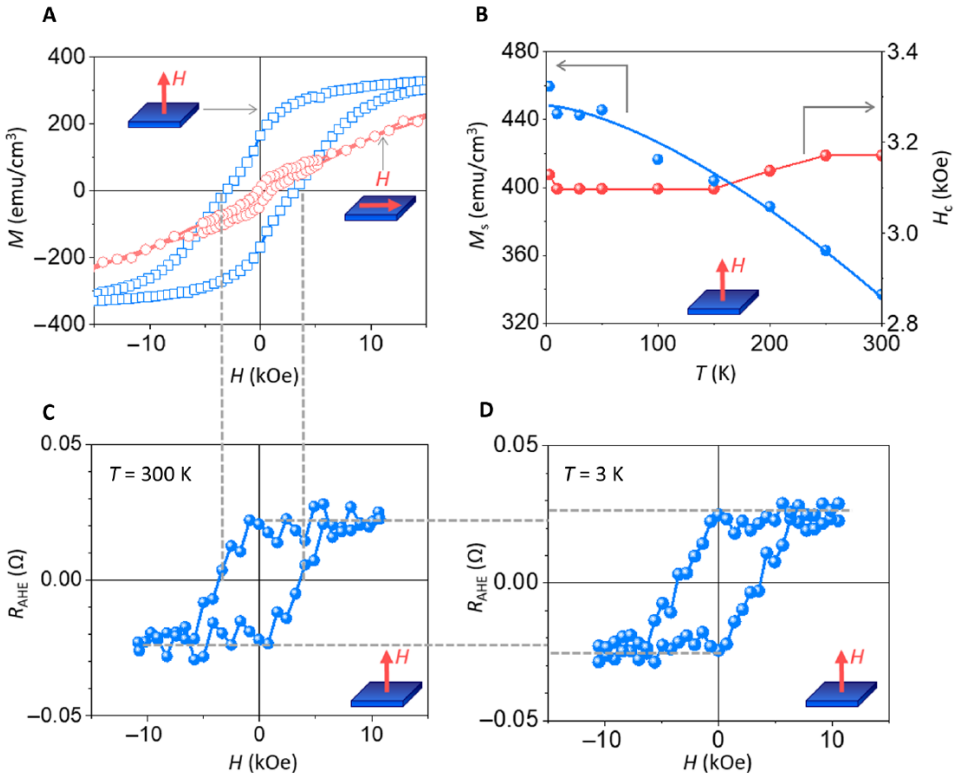

Fig. 2. Magnetic properties and AHE resistance of $Bi_2Se_3/BaFe_{12}O_{19}$. (**A**) Magnetization (*M*) vs. field (*H*) loops measured with the same $Bi_2Se_3/BaFe_{12}O_{19}$ sample as the one whose RHEED image is shown in Fig. 1B. (**B**) Saturation magnetization (M_s) and coercive field (H_c) as a function of *T* measured with the same $BaFe_{12}O_{19}$ film as the one whose XRD spectrum is shown in Fig. 1A. (**C** and **D**) R_{AHE} vs. field (*H*) loops measured at $T = 300$ K and $T = 3$ K, as indicated, using the Hall bar structure shown in Fig. 1C.

the red data points in Fig. 3B. The overall effect is a hysteresis loop in the R_{AHE} versus I_{dc} response. Figure 3 (B to D) presents the data measured at different *T*, as indicated. The data indicate that the switching current (I_{sw}) decreases with decreasing *T*. This is attributed to the presence of more pronounced TSSs in the Bi_2Se_3 film at low *T*, as discussed below. The data in Fig. 3 (D and E) were obtained with **H** along opposite directions. One can see that the two loops evolve in opposite manners; this result is the same as in previous SOT-driven switching experiments and is a characteristic of SOT switching (*4*, *5*, *7*).

Effects of SOT on field switching in $Bi_2Se_3/BaFe_{12}O_{19}$

Figure 4 presents the field switching data that further demonstrate the effects of τ_{SO}. The data were measured at a field applied at an angle of 45° away from the film normal. When $I_{dc} > 0$, τ_{SO} produces an effective field $\mathbf{H}_{SO+}$ that hinders the reversal of **M**, as illustrated in the insets of Fig. 4 (A and B), leading to a relatively wide magnetic hysteresis loop and a relatively large (H_{sw}) or coercive field (H_c). In stark contrast, when $I_{dc} < 0$, τ_{SO} gives rise to a field $\mathbf{H}_{SO-}$ that is in the opposite direction of $\mathbf{H}_{SO+}$ and thereby assists the reversal of **M**, resulting in a narrower loop and a lower H_{sw}. This effect is evidently shown by the data in Fig. 4 (A and B).

To better demonstrate the strength of τ_{SO} in the $Bi_2Se_3/BaFe_{12}O_{19}$ sample, we presented data obtained with a $Pt/BaFe_{12}O_{19}$ sample in Fig. 4C for direct comparison. One can easily see that the effect in $Pt/BaFe_{12}O_{19}$ is significantly weaker. Since the change of H_{sw} directly reflects the strength of τ_{SO}, one can define $\eta = \frac{H_{sw}(I_{dc}>0)-H_{sw}(I_{dc}<0)}{2 \mid I_{dc} \mid /(wt)}$ (w, Hall bar width; t, Bi_2Se_3 or Pt film thickness) as the efficiency of τ_{SO} in assisting the field switching, as in (*12*). This efficiency η enables a quantitative comparison of the SOT effects in the two samples. As shown in Fig. 4D, η in $Bi_2Se_3/BaFe_{12}O_{19}$ is comparable to that in $Pt/BaFe_{12}O_{19}$ at room temperature, indicating that the Bi_2Se_3 film behaves like a heavy metal film in terms of SOT production. With decreasing *T*, η increases in both samples but at very different rates. Specifically, when *T* is decreased from 300 to 3 K, η in $Pt/BaFe_{12}O_{19}$ increases by a factor of about 10, while η in $Bi_2Se_3/BaFe_{12}O_{19}$ increases by a factor of about 300. Such a big difference results from the gradual formation of strong TSSs in the Bi_2Se_3 film with a decrease in *T*, as discussed below. Furthermore, the data in Fig. 4D also indicate that (i) η in $Bi_2Se_3/BaFe_{12}O_{19}$ increases more rapidly at relatively low *T* than at high *T*. (ii) At $T = 3$ K, η in $Bi_2Se_3/BaFe_{12}O_{19}$ is about 30 times higher than that in $Pt/BaFe_{12}O_{19}$. The implications of these results are discussed below.

Remarks about SOT switching in $Bi_2Se_3/BaFe_{12}O_{19}$

Several remarks should be made about the switching data presented in Figs. 3 and 4. (i) It may be possible that the switching in the $BaFe_{12}O_{19}$ film is realized through domain wall motion, rather than magnetization rotation. The sheared shape of the hysteresis loops indicates the presence of an anisotropy distribution, and low-anisotropy sites may act as domain nucleation centers. If that is the case, then the above discussions about the roles of the SOT fields and the insets about the switching mechanisms in Figs. 3 and 4 would apply to nucleation sites and the reversal dynamics inside the domain walls. (ii) The magnitude of R_{AHE} presented in Fig. 3 is

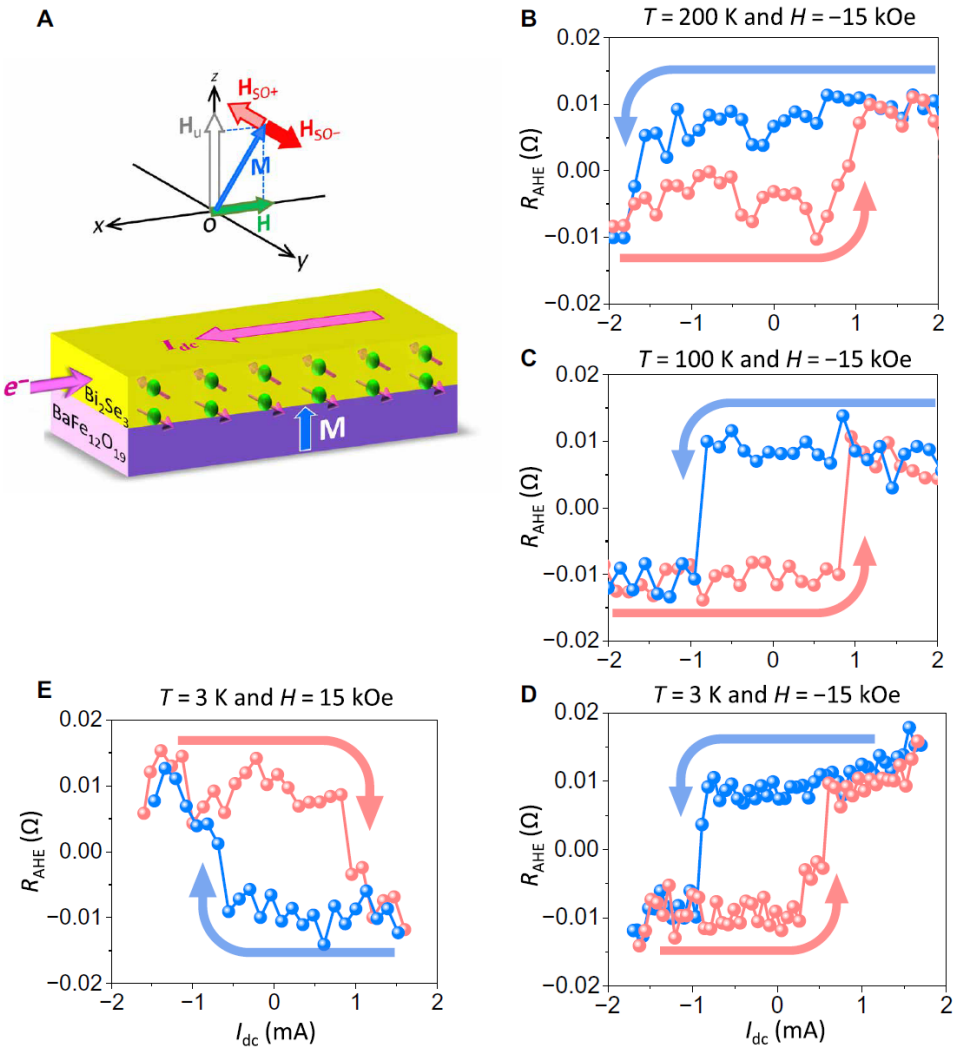

Fig. 3. SOT-induced switching in $Bi_2Se_3/BaFe_{12}O_{19}$. (**A**) Experimental configuration. (**B** to **E**) AHE resistance (R_{AHE}) measured as a function of charge current (I_{dc}) at different fields (H) and temperatures (T), as indicated. The arrows in (B) to (E) indicate the current sweeping directions.

smaller than that presented in Fig. 2. This is because, for the data in Fig. 3, an in-plane magnetic field was applied during the measurements, giving rise to a lower normal component of **M** than in the measurements of the data shown in Fig. 2. (iii) The loops in Fig. 3 are not centered along the I_{dc} axes. This was also observed in previous SOT switching studies (*10*, *12*). One possible reason for it is that the up-to-down and down-to-up switching involves different nucleation processes due to the presence of sample defects or field misalignment. (iv) The data in Fig. 4A indicate that after switching, R_{AHE} decreases when H increases from about 10 to 20 kOe. This is because at $H \approx 10$ kOe the equilibrium direction of **M** is in between **H** and $\mathbf{H}_u$, and an increase in H would pull **M** to rotate toward **H** and away from $\mathbf{H}_u$ and thereby results in a lower normal component of **M**. (v) The data in Fig. 4C show an unusual trend in the T dependence in comparison with the H_c data shown in Fig. 2B and the H_{sw} data shown in Fig. 4B, although the effects of I_{ac} are consistent at all Ts. This abnormal T dependence is most likely due to the drift of the measurement system, considering that three measurements were carried out using different I_{ac} at each after which T was changed to a different value. (vi) The enhancement of η in $Pt/BaFe_{12}O_{19}$ at low T was also previously observed in $Pt/Tm_3Fe_5O_{12}$ structures, wherein $Tm_3Fe_5O_{12}$ is an MI thin film with perpendicular anisotropy (*32*). As explained in (*32*), this low-T enhancement may result from the fact that higher M_s gives rise to a larger spin-mixing conductance at the interface.

DISCUSSION

The above-presented strong SOT effects at low T can be attributed to the presence of nontrivial TSS in the Bi_2Se_3 film. In principle, the TSS is present in the film over the entire measurement T range, but it is much more pronounced at low T due to enhanced surface state conductivity (σ_{TSS}) and reduced bulk state conductivity. The low-T enhancement of σ_{TSS} is discussed below; the decrease of the bulk conductivity at low T is shown in the inset of Fig. 1F and can be understood as a result of the shift of the E_F with T and the electron-electron interaction, as discussed earlier. The more dominant the TSS is, the more efficient the charge current-to-spin current conversion

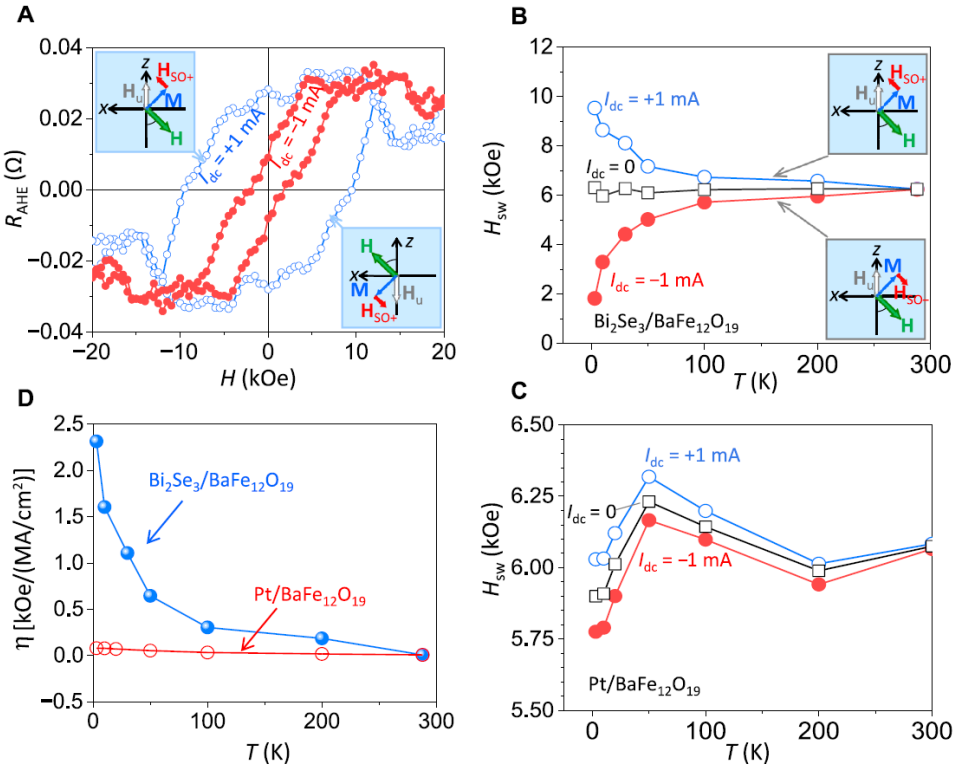

Fig. 4. Effects of SOT on field switching in $Bi_2Se_3/BaFe_{12}O_{19}$ and $Pt/BaFe_{12}O_{19}$. (**A**) Effects of I_{dc} on R_{AHE} hysteresis loops at $T = 3$ K in $Bi_2Se_3/BaFe_{12}O_{19}$. (**B**) Switching field (H_{sw}) as a function of T measured at different I_{dc}, as indicated, in $Bi_2Se_3/BaFe_{12}O_{19}$. (**C**) H_{sw} as a function of T measured at different I_{dc}, as indicated, in $Pt/BaFe_{12}O_{19}$. (**D**) SOT efficiency (η) as a function of T in $Bi_2Se_3/BaFe_{12}O_{19}$ and $Pt/BaFe_{12}O_{19}$. The data were all measured at a field applied at an angle of 45° away from the film normal direction. The data on $Pt/BaFe_{12}O_{19}$ were measured with a Hall bar structure that had the same dimension as the $Bi_2Se_3/BaFe_{12}O_{19}$ Hall bar.

is and the stronger the SOT is. The demonstrated low-T SOT enhancement is in a good agreement with previous T-dependent experiments on Bi_2Se_3 thin films (*33*). Through electric transport and spin-torque FM resonance measurements, those studies showed that the charge-to-spin conversion for TSSs in Bi_2Se_3 thin films became more efficient with a decrease in T.

The enhancement of σ_{TSS} at low T is mainly because the scattering of surface state electrons with phonons in the Bi_2Se_3 film becomes weaker as T decreases. A theoretical analysis, presented in the Supplementary Materials, indicates that σ_{TSS} exhibits a T^{-1} dependence when T is much higher than the Debye temperature Θ but a much stronger T^{-5} dependence in the low-T limit when $T << \Theta$. This T dependence is consistent with the T dependence of the SOT efficiency η shown in Fig. 4D, which shows that η increases slowly when T decreases from 300 to 100 K but much more rapidly from 100 to 3 K. A previous study has shown that Θ in Bi_2Se_3 films is about 180 K (*34*). Note that the strong T dependence of η cannot be explained by changes in the magnetic properties of the $BaFe_{12}O_{19}$ film, as shown by micromagnetic simulations presented in the Supplementary Materials.

The low-T SOT enhancement could also potentially arise from the enhanced spin-orbit coupling in the bulk because when T decreases, the bulk can evolve into a better conductor due to weakened electron-phonon scattering. This, however, is unlikely because when T is decreased from 3 K to 25 K and the conductivity decreases (see the inset of Fig. 1F), the SOT yet undergoes the most rapid increase (see Fig. 4B). Nevertheless, it is believed that the spin-orbit coupling in the bulk does contribute to the SOT, although its contribution should be smaller than the TSSs contribution at low T. Previous work has shown that, in comparison with the TSSs contribution, the bulk contribution is nontrivial for Bi_2Se_3 films thicker than 8 nm but is negligible in thinner films (*8*, *21*). The Bi_2Se_3 film in this work is 6 nm thick.

In addition to the TSSs and the spin-orbit coupling in the bulk states, there exists the Rashba spin splitting for the two-dimensional electron gas (2DEG) that also contributes to the generation of spin currents in the Bi_2Se_3 film. In that case, the 2DEG appears due to quantum confinement associated with the bending of the bulk bands at the film surfaces. The spin currents due to this Rashba effect, however, have opposite polarization to those produced by the TSSs and the bulk states (*7*, *12*). Thus, the effect partially cancels the spin currents generated by the TSSs, as reported previously (*35*), and therefore does not account for the observed low-T SOT enhancement.

Note that I_{sw} attains its smallest value (see Fig. 3) and η its largest (see Fig. 4D) at $T = 3$ K, which is the lowest T used in this work. Even smaller I_{sw} and larger η are expected with a further decrease in T.

It is important to highlight that the data in Figs. 3 (D and E) and 4A represent the first unambiguous demonstration of TSS-driven magnetization switching. As mentioned above, the SOT switching in recent studies on TI/FM systems (*6*–*12*) may not be TSS-driven because interfacing a TI layer with a conductive FM film can significantly modify or even completely suppress the TSSs in the TI layer (*14*–*18*). In contrast, the $BaFe_{12}O_{19}$ layer in this work is an MI, which is expected to produce negligible effects on the TSSs (*16*). It is predicted that the only notable effect due to the proximity to an MI film is the opening of a very small gap at the Dirac point of the TI film (*16*). This gap opening, if it exists, has no effect on the SOT

switching present above because the E_F is well above the Dirac point in the sample studied here (see the inset of Fig. 1E).

Note that there exists a magnetoelectric effect in $BaFe_{12}O_{19}$, but this effect is not responsible for the observed magnetization switching for two reasons. First, in contrast to the Y-type and Z-type hexagonal ferrites that show strong multiferroic effects, the magnetoelectric effect in $BaFe_{12}O_{19}$, an M-type hexagonal ferrite, is weak (*36*–*38*). Second, during the switching experiments, there is no apparent electric field across the $BaFe_{12}O_{19}$ film, since the bottom sapphire substrate is electrically insulating and the electric current flows only in the top Bi_2Se_3 layer. Very different switching responses in the $Bi_2Se_3/BaFe_{12}O_{19}$ and $Pt/BaFe_{12}O_{19}$ (see Fig. 4D) samples indicate that the switching is not due to the magnetoelectric effect in the $BaFe_{12}O_{19}$ film. One would expect similar responses in the two samples if the switching is driven by the magnetoelectric effect.

Last, it should be mentioned that a section on the estimation of the charge-to-spin conversion efficiency and the SOT strength in the $Bi_2Se_3/BaFe_{12}O_{19}$ structures has been included in the Supplementary Materials. Because of the presence of the TSSs, the estimated spin Hall angle (θ_{SH}), inverse Edelstein effect length (λ_{IEE}), and SOT fields (H_{SO}) at 3 K are larger than the corresponding values reported previously for Bi_2Se_3/"FM metal" bilayered structures.

MATERIALS AND METHODS

Material growth

The $BaFe_{12}O_{19}$ thin films were grown on (0001)-oriented Al_2O_3 substrates (CRYSTAL GmbH) using a pulsed laser deposition (PLD) system with a base pressure of 2×10^{-7} torr (*3*). The PLD system used a 248-nm KrF excimer laser, and the energy fluence of the laser beam was 1.7 J/cm^2. The target-to-substrate distance was set to 5 cm. The $BaFe_{12}O_{19}$ target was preablated, while the T ramped up to 800°C. During the deposition, the oxygen pressure was kept at 75 mtorr. The laser pulse rate ramped from 1 to 5 pulse/s with equal steps during the initial 5 min, and it was kept at 5 pulse/s for the rest, which corresponds to a film growth rate of about 2.5 Å/min. The film was annealed in situ at 800°C in 400-torr oxygen for 10 min and was then cooled to room temperature at a rate of 2°C/min.

The growth of the Bi_2Se_3 film was performed in a molecular beam epitaxy (MBE) system with a base pressure of 2×10^{-10} torr or lower. High-purity Se (99.999%) and Bi (99.999%) targets were supplied from solid sources in Knudsen cells to maintain a flux ratio of 16.8:1. Before the growth, the $BaFe_{12}O_{19}$ film was heated to 340°C first. The T was subsequently reduced to 225°C, and at this T, a Bi_2Se_3 buffer layer (<1 nm) was deposited for 90 s to facilitate growth. The film T was then increased to 290°C. Once at this T, Bi_2Se_3 deposition continued at 2.34 Å/min, while the T continually ramped to an ultimate T of 320°C. After cooling the film to room T, a thin Te capping layer (~2 nm) was deposited using Te (99.9999%) also from a Knudsen cell to prevent the oxidization of the Bi_2Se_3 film.

The Pt layer was deposited in a magnetron sputtering system with a base pressure of 2×10^{-8} torr. The deposition was at room temperature, and the deposition rate was about 0.33 Å/s.

Device fabrication

Standard nanofabrication procedures were used to pattern the $Bi_2Se_3/BaFe_{12}O_{19}$ and $Pt/BaFe_{12}O_{19}$ samples. The samples were patterned into 10-μm-wide Hall bars in a photolithography system first and were then etched in an argon ion milling system. Contact pads of Ti (5 nm)/Au (150 nm) were deposited for electrical measurements.

Characterization

The crystalline structure and thickness of the $BaFe_{12}O_{19}$ film were characterized by a Rigaku SmartLab XRD/XRR (x-ray reflectivity) system. A MicroSense EV7 vibrating sample magnetometer (VSM) and a Quantum Design DynaCool VSM were used to measure the magnetization curves at different T. After the Bi_2Se_3 film was grown on the $BaFe_{12}O_{19}$ film in the MBE system, RHEED was performed in situ to examine the crystalline structure of the Bi_2Se_3 film.

Electrical measurements

Hall measurements were conducted in two Quantum Design physical property measurement systems. A Keithley 6221 current source was used to generate alternating currents and pulsed direct currents, and two SR830 lock-in amplifiers and an SR560 preamplifier were used to measure the Hall voltage of the Hall bars. The alternating current with a root mean square amplitude of 0.05 mA was used to measure the Hall responses. The pulsed direct currents for switching measurements had an amplitude of 1 mA and a time duration of 5 ms. To eliminate the effect of Joule heating, each data point was taken after pausing for 60 to 180 s after a direct current pulse was applied.

SUPPLEMENTARY MATERIALS

Supplementary material for this article is available at http://advances.sciencemag.org/cgi/content/full/5/8/eaaw3415/DC1

Section S1. Anti-weak localization
Section S2. T dependence of SOT
Section S3. Micromagnetic simulations of SOT-induced magnetization switching
Section S4. Estimation of SOT strength
Section S5. Estimation of fermi level and carrier density
Section S6. Cross-section image of $Bi_2Se_3/BaFe_{12}O_{19}$
Fig. S1. Dependence of the conductivity of the Bi_2Se_3 film on a magnetic field applied along the film normal direction.
Fig. S2. Simulated results on SOT-induced switching at $T = 0$ K and $T = 300$ K.
Fig. S3. Simulated results on SOT-assisted field switching under the configuration are the same as that for Fig. 4 in the main text.
Fig. S4. Estimation of strength of SOC and SOT in $Bi_2Se_3/BaFe_{12}O_{19}$.
Fig. S5. Calculated E_F and carrier densities.
Fig. S6. High-resolution transmission electron microscopy image of the $Bi_2Se_3/BaFe_{12}O_{19}$ stack with Te capping layer.
References (*39*, *40*)

REFERENCES AND NOTES

1. I. M. Miron, G. Gaudin, S. Auffret, B. Rodmacq, A. Schuhl, S. Pizzini, J. Vogel, P. Gambardella, Current-driven spin torque induced by the Rashba effect in a ferromagnetic metal layer. *Nat. Mater.* **9**, 230–234 (2010).
2. L. Liu, C.-F. Pai, Y. Li, H. W. Tseng, D. C. Ralph, R. A. Buhrman, Spin torque switching with the giant spin Hall effect of tantalum. *Science* **336**, 555–558 (2012).
3. P. Li, T. Liu, H. Chang, A. Kalitsov, W. Zhang, G. Csaba, W. Li, D. Richardson, A. DeMann, G. Rimal, H. Dey, J. S. Jiang, W. Porod, S. B. Field, J. Tang, M. C. Marconi, A. Hoffmann, O. Mryasov, M. Wu, Spin-orbit torque-assisted switching in magnetic insulator thin films with strong perpendicular magnetic anisotropy. *Nat. Commun.* **7**, 12688 (2016).
4. S. Emori, U. Bauer, S.-M. Ahn, E. Martinez, G. S. D. Beach, Current-driven dynamics of chiral ferromagnetic domain walls. *Nat. Mater.* **12**, 611–616 (2013).
5. Z. Duan, A. Smith, L. Yang, B. Youngblood, J. Lindner, V. E. Demidov, S. O. Demokritov, I. N. Krivorotov, Nanowire spin torque oscillator driven by spin orbit torques. *Nat. Commun.* **5**, 5616 (2014).
6. Y. Fan, P. Upadhyaya, X. Kou, M. Lang, S. Takei, Z. Wang, J. Tang, L. He, L.-T. Chang, M. Montazeri, G. Yu, W. Jiang, T. Nie, R. N. Schwartz, Y. Tserkovnyak, K. L. Wang, Magnetization switching through giant spin–orbit torque in a magnetically doped topological insulator heterostructure. *Nat. Mater.* **13**, 699–704 (2014).
7. J. Han, A. Richardella, S. A. Siddiqui, J. Finley, N. Samarth, L. Liu, Room-temperature spin-orbit torque switching induced by a topological insulator. *Phys. Rev. Lett.* **119**, 077702 (2017).

8. Y. Wang, D. Zhu, Y. Wu, Y. Yang, J. Yu, R. Ramaswamy, R. Mishra, S. Shi, M. Elyasi, K.-L. Teo, Y. Wu, H. Yang, Room temperature magnetization switching in topological insulator-ferromagnet heterostructures by spin-orbit torques. *Nat. Commun.* **8**, 1364 (2017).
9. K. Yasuda, A. Tsukazaki, R. Yoshimi, K. Kondou, K. S. Takahashi, Y. Otani, M. Kawasaki, Y. Tokura, Current-nonlinear Hall effect and spin-orbit torque magnetization switching in a magnetic topological insulator. *Phys. Rev. Lett.* **119**, 137204 (2017).
10. Y. Li, Q. Ma, S. X. Huang, C. L. Chien, Thin films of topological Kondo insulator candidate SmB_6: Strong spin-orbit torque without exclusive surface conduction. *Sci. Adv.* **4**, eaap8294 (2018).
11. M. Dc, R. Grassi, J.-Y. Chen, M. Jamali, D. R. Hickey, D. Zhang, Z. Zhao, H. Li, P. Quarterman, Y. Lv, M. Li, A. Manchon, K. A. Mkhoyan, T. Low, J.-P. Wang, Room-temperature high spin–orbit torque due to quantum confinement in sputtered $Bi_xSe_{(1-x)}$ films. *Nat. Mater.* **17**, 800–807 (2018).
12. N. H. D. Khang, Y. Ueda, P. N. Hai, A conductive topological insulator with large spin Hall effect for ultralow power spin–orbit torque switching. *Nat. Mater.* **17**, 808–813 (2018).
13. C.-F. Pai, Switching by topological insulators. *Nat. Mater.* **17**, 755–757 (2018).
14. L. A. Wray, S.-Y. Xu, Y. Xia, D. Hsieh, A. V. Fedorov, Y. S. Hor, R. J. Cava, A. Bansil, H. Lin, M. Z. Hasan, A topological insulator surface under strong Coulomb, magnetic and disorder perturbations. *Nat. Phys.* **7**, 32–37 (2011).
15. J.-C. Rojas-Sánchez, S. Oyarzún, Y. Fu, A. Marty, C. Vergnaud, S. Gambarelli, L. Vila, M. Jamet, Y. Ohtsubo, A. Taleb-Ibrahimi, P. Le Fèvre, F. Bertran, N. Reyren, J.-M. George, A. Fert, Spin to charge conversion at room temperature by spin pumping into a new type of topological insulator: α-Sn films. *Phys. Rev. Lett.* **116**, 096602 (2016).
16. J. Zhang, J. P. Velev, X. Dang, E. Y. Tsymbal, Band structure and spin texture of Bi_2Se_3 3*d* ferromagnetic metal interface. *Phys. Rev. B* **94**, 014435 (2016).
17. J. M. Marmolejo-Tejada, K. Dolui, P. Lazić, P.-H. Chang, S. Smidstrup, D. Stradi, K. Stokbro, B. K. Nikolić, Proximity band structure and spin textures on both sides of topological-insulator/ferromagnetic-metal interface and their charge transport probes. *Nano Lett.* **17**, 5626–5633 (2017).
18. Y.-T. Hsu, K. Park, E.-A. Kim, Hybridization-induced interface states in a topological insulator-magnetic metal heterostructure. *Phys. Rev. B* **96**, 235433 (2017).
19. R. Singh, K. K. Shukla, A. Kumar, G. S. Okram, D. Singh, V. Ganeshan, A. Lakhani, A. K. Ghosh, S. Chatterjee, Large power factor and anomalous Hall effect and their correlation with observed linear magneto resistance in Co-doped Bi_2Se_3 3D topological insulator. *J. Phys. Condens. Matter* **28**, 376001 (2016).
20. H. Grahn, *Introduction to Semiconductor Physics* (World Scientific, ed. 1, 2001).
21. C. H. Li, O. M. J. van 't Erve, J. T. Robinson, Y. Liu, L. Li, B. T. Jonker, Electrical detection of charge-current-induced spin polarization due to spin-momentum locking in Bi_2Se_3. *Nat. Nanotechnol.* **9**, 218–224 (2014).
22. M. Liu, C.-Z. Chang, Z. Zhang, Y. Zhang, W. Ruan, K. He, L.-l. Wang, X. Chen, J.-F. Jia, S.-C. Zhang, Q.-K. Xue, X. Ma, Y. Wang, Electron interaction-driven insulating ground state in Bi_2Se_3 topological insulators in the two-dimensional limit. *Phys. Rev. B* **83**, 165440 (2011).
23. J. Wang, A. M. DaSilva, C.-Z. Chang, K. He, J. K. Jain, N. Samarth, X.-C. Ma, Q.-K. Xue, M. H. W. Chan, Evidence for electron-electron interaction in topological insulator thin films. *Phys. Rev. B* **83**, 245438 (2011).
24. H.-Z. Lu, S.-Q. Shen, Weak localization and weak anti-localization in topological insulators. *Proc. SPIE* **9167**, 91672E (2014).
25. J. Chen, H. J. Qin, F. Yang, J. Liu, T. Guan, F. M. Qu, G. H. Zhang, J. R. Shi, X. C. Xie, C. L. Yang, K. H. Wu, Y. Q. Li, L. Lu, Gate-voltage control of chemical potential and weak antilocalization in Bi_2Se_3. *Phys. Rev. Lett.* **105**, 176602 (2010).
26. Q. Hao, G. Xiao, Giant spin Hall effect and magnetotransport in a Ta/CoFeB/MgO layered structure: A temperature dependence study. *Phys. Rev. B* **91**, 224413 (2015).
27. M. Lang, M. Montazeri, M. C. Onbasli, X. Kou, Y. Fan, P. Upadhyaya, K. Yao, F. Liu, Y. Jiang, W. Jiang, K. L. Wong, G. Yu, J. Tang, T. Nie, L. He, R. N. Schwartz, Y. Wang, C. A. Ross, K. L. Wang, Proximity induced high-temperature magnetic order in topological insulator - ferrimagnetic insulator heterostructure. *Nano Lett.* **14**, 3459–3465 (2014).
28. F. Katmis, V. Lauter, F. S. Nogueira, B. A. Assaf, M. E. Jamer, P. Wei, B. Satpati, J. W. Freeland, I. Eremin, D. Heiman, P. Jarillo-Herrero, J. S. Moodera, A high-temperature ferromagnetic topological insulating phase by proximity coupling. *Nature* **533**, 513–516 (2016).
29. C. Tang, C.-Z. Chang, G. Zhao, Y. Liu, Z. Jiang, C.-X. Liu, M. R. McCartney, D. J. Smith, T. Chen, J. S. Moodera, J. Shi, Above 400-K robust perpendicular ferromagnetic phase in a topological insulator. *Sci. Adv.* **3**, e1700307 (2017).
30. Y.-T. Chen, S. Takahashi, H. Nakayama, M. Althammer, S. T. B. Goennenwein, E. Saitoh, G. E. W. Bauer, Theory of spin Hall magnetoresistance. *Phys. Rev. B* **87**, 144411 (2013).
31. S. S.-L. Zhang, G. Vignale, Nonlocal anomalous Hall effect. *Phys. Rev. Lett.* **116**, 136601 (2016).
32. Q. Shao, C. Tang, G. Yu, A. Navabi, H. Wu, C. He, J. Li, P. Upadhyaya, P. Zhang, S. A. Razavi, Q. L. He, Y. Liu, P. Yang, S. K. Kim, C. Zheng, Y. Liu, L. Pan, R. K. Lake, X. Han, Y. Tserkovnyak, J. Shi, K. L. Wang, Role of dimensional crossover on spin-orbit torque efficiency in magnetic insulator thin films. *Nat. Commun.* **9**, 3612 (2018).
33. Y. Wang, P. Deorani, K. Banerjee, N. Koirala, M. Brahlek, S. Oh, H. Yang, Topological surface states originated spin-orbit torques in Bi_2Se_3. *Phys. Rev. Lett.* **114**, 257202 (2015).
34. X. Chen, H. D. Zhou, A. Kiswandhi, I. Miotkowski, Y. P. Chen, P. A. Sharma, A. L. Lima Sharma, M. A. Hekmaty, D. Smirnov, Z. Jiang, Thermal expansion coefficients of Bi_2Se_3 and Sb_2Te_3 crystals from 10 K to 270 K. *Appl. Phys. Lett.* **99**, 261912 (2011).
35. S. Shi, A. Wang, Y. Wang, R. Ramaswamy, L. Shen, J. Moon, D. Zhu, J. Yu, S. Oh, Y. Feng, H. Yang, Efficient charge-spin conversion and magnetization switching through the Rashba effect at topological-insulator/Ag interfaces. *Phys. Rev. B* **97**, 041115(R) (2018).
36. Y. Tokunaga, Y. Kaneko, D. Okuyama, S. Ishiwata, T. Arima, S. Wakimoto, K. Kakurai, Y. Taguchi, Y. Tokura, Multiferroic M-type hexaferrites with a room-temperature conical state and magnetically controllable spin helicity. *Phys. Rev. Lett.* **105**, 257201 (2010).
37. S.-P. Shen, Y.-S. Chai, J.-Z. Cong, P.-J. Sun, J. Lu, L.-Q. Yan, S.-G. Wang, Y. Sun, Magnetic-ion-induced displacive electric polarization in FeO_5 bipyramidal units of $(Ba,Sr)Fe_{12}O_{19}$ hexaferrites. *Phys. Rev. B* **90**, 180404(R) (2014).
38. Y. S. Chai, S. H. Chun, J. Z. Cong, K. H. Kim, Magnetoelectricity in multiferroic hexaferrites as understood by crystal symmetry analyses. *Phys. Rev. B* **98**, 104416 (2018).
39. H. Wang, J. Kally, J. S. Lee, T. Liu, H. Chang, D. R. Hickey, K. A. Mkhoyan, M. Wu, A. Richardella, N. Samarth, Surface-state-dominated spin-charge current conversion in topological-insulator–ferromagnetic-insulator heterostructures. *Phys. Rev. Lett.* **117**, 076601 (2016).
40. N. Bansal, Y. S. Kim, M. Brahlek, E. Edrey, S. Oh, Thickness-independent transport channels in topological insulator Bi_2Se_3 thin films. *Phys. Rev. Lett.* **109**, 116804 (2012).

Acknowledgments

Funding: The fabrication and characterization of the samples and the electrical measurements were supported mainly by the U.S. National Science Foundation under grant no. EFMA-1641989. The data analyses were supported mainly by the U.S. Department of Energy, Office of Science, Basic Energy Sciences under award DE-SC0018994. Work at PSU was supported by the Pennsylvania State Two-Dimensional Crystal Consortium-Materials Innovation Platform (2DCC-MIP) under the U.S. National Science Foundation grant no. DMR-1539916. Work at Argonne was supported by the U.S. Department of Energy, Office of Science, Basic Energy Sciences, Materials Science and Engineering Division. Work at UW was supported by the U.S. National Science Foundation under grant no. DMR-1710512. Work at Arizona was supported by the NSF under grant no. ECCS-1554011. **Author contributions:** P.L. and M.W. conceived the idea and designed the experiments. P.L. and Jinjun Ding grew and characterized $BaFe_{12}O_{19}$ films. J.K., T.P., and N.S. grew and characterized Bi_2Se_3 films. Y.L. and R.S. contributed to TEM characterizations. Junjia Ding, C.B., A.D., S.B.F., W.W., and V.N. contributed to device fabrications. P.L., Jinjun Ding, and G.R. performed measurements. J.K., T.P., J.S.J., C.B., W.Z., J.T., A.H., N.S., and M.W. contributed to measurements and data analyses. S.S.-L.Z. and O.G.H. carried out theoretical analyses. G.C. performed micromagnetic simulations. M.W. supervised the study. P.L., S.S.-L.Z., G.C., and M.W. wrote the paper and the Supplementary Materials with help from all the other co-authors. **Competing interests:** The authors declare that they have no competing interests. **Data and materials availability:** All data needed to evaluate the conclusions in the paper are present in the paper and/or the Supplementary Materials. Additional data related to this paper may be requested from the authors.

Submitted 11 December 2018
Accepted 31 July 2019
Published 30 August 2019
10.1126/sciadv.aaw3415

Citation: P. Li, J. Kally, S. S.-L. Zhang, T. Pillsbury, J. Ding, G. Csaba, J. Ding, J. S. Jiang, Y. Liu, R. Sinclair, C. Bi, A. DeMann, G. Rimal, W. Zhang, S. B. Field, J. Tang, W. Wang, O. G. Heinonen, V. Novosad, A. Hoffmann, N. Samarth, M. Wu, Magnetization switching using topological surface states. *Sci. Adv.* **5**, eaaw3415 (2019).